ACS APPLIED MATERIALS & INTERFACES

Research Article

www.acsami.org

Preparation and Electromagnetic Properties of Core/Shell Polystyrene@Polypyrrole@Nickel Composite Microspheres

Wenzhe Li, Teng Qiu,* Leilei Wang, Shanshan Ren, Jiangru Zhang, Lifan He, and Xiaoyu Li*

College of Materials Science and Engineering, State Key Laboratory of Organic−Inorganic Composites, Key Laboratory of Carbon Fiber and Functional Polymers, Ministry of Education, Beijing Engineering Research Center of Syntheses and Applications of Waterborne Polymers, Beijing University of Chemical Technology, Beijing, 100029, China

Supporting Information

ABSTRACT: Through a novel method, we successfully synthesized electromagnetic (EM) functional polystyrene@polypyrrole@nickel (PS@PPy@Ni) composite microspheres. The PS@PPy spheres with well-defined core/shell structure have been synthesized via an in situ chemical oxidative copolymerization of pyrrole (Py) and *N*-2-carboxyethylpyrrole (PyCOOH) templated by PS microspheres. The reaction was carried out under heterophase conditions using the mixture of ethanol and water as the continuous phase. Tailored by the carboxyl groups on the surface of microspheres, magnetic nickel layer has been steady deposited onto the P(Py-PyCOOH) layer of the microspheres through an activation-electroless plating technology. The fine PS@P(Py-PyCOOH)@Ni core/shell structures could be obtained with the PyCOOH content up to 50 wt % in the P(Py-PyCOOH) layer. Moreover, the as-prepared PS@P(Py-PyCOOH)@Ni composites are ferromagnetic materials and behave as a good electromagnetic (EM) absorption material due to the coating of Ni layer around the PS@P(Py-PyCOOH) spheres. The PS@P(Py-PyCOOH)@Ni composite spheres show the remarkable EM wave absorption property with the maximum reflection loss (around −20.06 dB) at 10.69 GHz. The EM wave absorption can retained lower than −10 dB within a broad frequency range from 9.16 to 13.75 GHz.

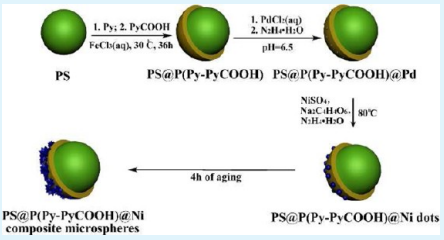

KEYWORDS: *functional polymer microspheres, polypyrole, nickel, core/shell, electromagnetic wave absorption*

1. INTRODUCTION

During the past decade, composite spheres of conductive polymer and nanometal with the dimension from nanoscale to microscale have attracted great attentions, which combine the mechanical flexibility, optical and electrical properties of conducting polymers with the high electrical conductivity and magnetic properties of metals.[1−3] Many fabrication methods have been reported for the preparation of organic/inorganic hybrid functional materials with sphere morphology.[4−7] The modification on the interfacial phase between polymer and inorganic metals is essential for the construction of composite microstructures.[8−20] To improve the applicability of polymer/inorganic metal composites, researchers have also employed multicomponent system to fabricate the microspheres.[21−23] For example, Zhang et al.[23] reported the synthesis of polystyrene@polypyrrole@nano Ag (PS@PPy@Ag) composite particles via an in situ redox polymerization templated by PS latex particles. And inducing the PS latex particle as the core of the composite microspheres can effectively narrow the size distribution, decrease the weight, and improve the processability for the PS@PPy@Ag composite particles. Moreover, for the monodisperse composite microspheres, there are many practical applications, such as electronic package, catalysis, nanodevices, magnetic recording media, electromagnetic (EM) interference shielding materials, protection of biologically active agents, and hydrogen storage, depending on their compositions and microstructures.[24−37]

On the basis of conducting polymers such as PPy and magnetic nanometals, EM-functionalized micro/nanocomposites can be prepared to improve the properties of the material, such as electromagnetic shielding (EMS), microwave adsorption, magnetic resonance image (MRI) enhancement, and drug targeting.[38] Several groups have reported their studies on the nanocomposites with Co,[39] Fe_3O_4,[40−42] or Ni nanoparticles[43] encapsulated by PPy or polyaniline (PANI) shell. The interface between metal and conductive polymer shows a great contribution on the complex permittivity (ε_r) of composite materials. It has been well-accepted that the reflection and attenuation of EM wave in a material is determined by the relative complex permittivity ($\varepsilon_r = \varepsilon' + j\tilde{\varepsilon}$), relative complex permeability ($\mu_r = \mu' + j\tilde{\mu}$), and the electromagnetic impedance matching, depending on the component and structure of the material.[44] The addition of good dielectric performance of conductive polymers such as PPy together with magnetic performance of magnetite such as metal nickel (Ni) can effectively improve the EM wave reflection loss of composite sphere. Meanwhile, construction of a core/shell structure can further contribute on additional interfacial dielectric relaxation.[45] However, only several literatures have been reported on the magnetite/conductive polymer composites,[38,46] and there is

Received: November 2, 2012
Accepted: December 31, 2012
Published: December 31, 2012

still no report focused on core/shell microspheres of (nonconductive polymer)/(conductive polymer)/(magnetic metal) multilayer structure. The work in the preparation and exploration on the EM properties of such composite microspheres should be helpful for the design of novel EM wave absorption materials to decrease the density and improve the controllability. Moreover, additional interfacial relaxation loss can also be expected via the formation of multilayer structures on which the knowledge about the EM properties is still very limited.

Recently, we synthesized the PS@PPy core/shell microspheres and hollow capsules via an in situ oxidative polymerization of pyrrole (Py) using $FeCl_3 \cdot 6H_2O$ as the oxidizer in an aqueous emulsion of PS latex.[47] Such PS@PPy microspheres with the core/shell structure and narrow particle size distribution should be available as a precursor for us to fabricate the PS@PPy@magnetic metal multilayer core/shell composite microspheres via the further postdeposition of nanometal layer onto the outmost surface of PPy layer. The sole PS spheres have no EM wave absorption property. PS in the composite spheres serves as the template for the formation of composite core/shell spheres, which would benefit for EM wave absorption owing to the multiple reflections in the conductive cavity and the interface relaxation.

Because the formation of a stable metal layer outside the PPy layer of the composite microsphere is important for their final EM properties, functional groups such as carboxyl acid groups are necessary to be introduced on PPy layer, which can stabilize the metal particles attached on the PPy surface. It has been reported that 1-(2-carboxyethyl) pyrrole (PyCOOH) can be copolymerized with pyrrole so as to induce the carboxyl groups on PPy film surface.[48,49] Therefore, in this study, we induced PyCOOH as the functional monomer to copolymerize with PPy during the synthesis of PS@PPy core/shell microspheres, which were further employed to prepare the PS@PPy@magnetic metal microspheres. Moreover, we chose Ni as the magnetic metal which is relatively cheap, stable and can be in situ prepared by the activation-electroless plating method.

On the basis of the discussion above, in this work, the PS@P(Py-PyCOOH)@Ni core/shell composite microspheres were prepared by a three-step method as sketched in Scheme 1. In the first step, the PS@P(Py-PyCOOH) core−shell microspheres were synthesized via an in situ oxidative copolymerization of Py and PyCOOH templated by PS microspheres, so as to induce the carboxyl acid groups in the P(Py-PyCOOH) layer. In the second step, nano Pd was in situ produced by the reduction reaction of $PdCl_2$ and hydrazine, and the carboxyl acid groups in the P(Py-PyCOOH) layer could effectively provide the binding sites for the load of nano Pd particles onto the PS@P(Py-PyCOOH) core−shell spheres. These loaded Pd nano particles could activate the reduction reaction of Ni complex ion and hydrazine. Finally, the Ni metal was reduced and uniformly deposited onto the activated spheres for the formation of the Ni layer via the electroless plating technology. Morphology and structure of the as-synthesized microspheres during each step were investigated by using scanning electron microscope (SEM), transmission electron microscopy (TEM), high-resolution TEM (HRTEM), energy-dispersive X-ray (EDX) analysis, X-ray diffraction (XRD), and thermogravimetric analyzer (TGA). Furthermore, the influence of PyCOOH content in the P(Py-PyCOOH) layer on the magnetic properties and the EM wave absorption performance of the PS@P(Py-PyCOOH)@Ni composite microspheres was revealed in detail. The results indicated that the continuous Ni layer could be only obtained as high PyCOOH content in the P(Py-PyCOOH) layer, which in turn resulted in the obviously enhanced EM wave absorption performance.

Scheme 1. Schematic Depiction of the Synthesis Procedure of PS@P(Py-PyCOOH)@Ni Core/Shell Microspheres

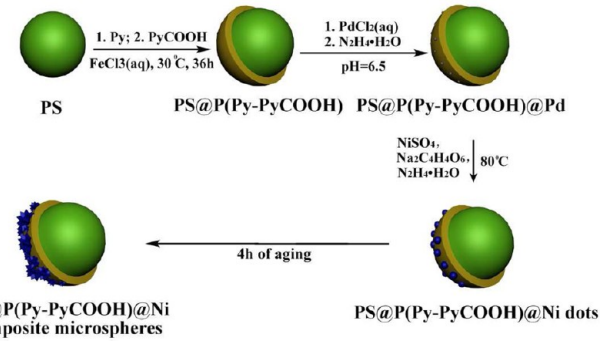

2. EXPERIMENTAL SECTION

2.1. Materials. Py, $PdCl_2$, and 1-(2-cyanoethyl) pyrrole (PyCN) were purchased from Aldrich and used as received. PPyCOOH was synthesized by reaction of PyCN and KOH as described in the literature.[48] Styrene (St), $FeCl_3 \cdot 6H_2O$, hydrazine ($N_2H_4 \cdot H_2O$, 80 wt %), $NiSO_4 \cdot 6H_2O$, sodium citrate, sodium tartaric ($Na_2C_4H_4O_6 \cdot 2H_2O$), ethanol, polyvinylpyrolidone (PVP, K-30), KOH, ethanol, and *p*-toluenesulfonic acid sodium salt ($C_7H_8O_3S$) were commercial analytical reagents and used without further purification. α-Azoisobutyronitrile (AIBN) used after recrystallization twice by ethanol. All the aqueous solutions were prepared with deionized water made in our lab.

2.2. Synthesis of Monodispersed PS Microsphere. The synthesis of monodisperse PS microspheres was carried out by dispersion polymerization, according to the literature.[50] The procedure was indicated as follow: St (19.50 g), PVP (1.17 g), AIBN (0.0975 g), ethanol (206.3 mL), and water (18.00 mL) were added into a 500 mL four necked round-bottom flask equipped with an agitator, thermometer and inert gas circulation. The solution was purges with nitrogen and then heated to 70 °C in a thermostatted water bath for 12 h. The polymer dispersion had 8 wt % solid content. PS microspheres (1.6 μm in diameter) were separated by three centrifugation/redispersion cycles in ethanol. Finally, the white solid was obtained after dried at 60 °C for 24 h.

2.3. Synthesis of PS@P(Py-PyCOOH) Core/Shell Microsphere. The dry PS microspheres (3.20 g) and PVP (0.32 g) were first dispersed in 8.0 mL of ethanol under ultrasonication. The dispersion was transferred into a 250 mL round-bottom flask contained 35 mL of aqueous solution of *p*-toluenesulfonic acid (6.6 wt %) and equipped with a magnetic stirrer. The temperature of reaction system was controlled at 30 °C by using water bath, and then the first batch of Py monomer in solution A1 (shown in Table 1) was added dropwise into the dispersion. Subsequently, the reaction was initiated via the oxidant solution A2 (shown in Table 1), which was slowly added into the reaction system within 4 h. Then the solutions of Py/PyCOOH (B1) (20 mL) and $FeCl_3 \cdot 6H_2O$ of B2 (20 mL) (both shown in Table 1) were synchronously dropped into the reaction system within 8 h. Finally, the reaction was carried out for another 12 h. The product was isolated by five centrifugation/redispersion cycles using deionized water. The PS@P(Py-PyCOOH) core/shell microspheres, where the P(Py-PyCOOH) layer was prepared with different mole percentage of PyCOOH component, were dried in an oven settled at 60 °C for 24 h and obtained as black powder with metallic gloss. For the sake of convenience, the P(Py-PyCOOH) layer with different compositions are designated hereafter as "P(Py-PyCOOH$_X$)", where X stands for molar radio of PyCOOH component in this layer.

dx.doi.org/10.1021/am302551d | ACS Appl. Mater. Interfaces 2013, 5, 883−891

Table 1. Composition of Solution for Preparing PS@P(Py-PyCOOH) Core/Shell Microspheres

		solution A1			solution A2		solution B1			solution B2	
sample no.	PyCOOH content[a] (%)	pyrrole (mmol)	CH_2Cl_2 (mL)	ethanol (mL)	$FeCl_3{\cdot}6H_2O$ (mmol)	H_2O (mL)	pyrrole (mmol)	PyCOOH (mmol)	H_2O (mL)	$FeCl_3{\cdot}6H_2O$ (mmol)	H_2O (mL)
PS@P(Py-$PyCOOH_0$)	0	11.49	0.43	5.0	26.8	25.0	0	0	0	0	0
PS@P(Py-$PyCOOH_{25}$)	25	8.13	0.43	5.0	18.9	5.0	0.56	2.88	20.0	8.0	20.0
PS@P(Py-$PyCOOH_{50}$)	50	4.77	0.43	5.0	11.1	5.0	0.98	5.76	20.0	15.7	20.0

[a]The molar radio of PyCOOH in monomer composition.

2.4. Synthesis of PS@P(Py-PyCOOH)@Ni Composite Microsphere. The synthesis of PS@P(Py-PyCOOH)@Ni composite microspheres was sequentially carried out by activation and incorporation of Ni as indicated bellow. (i) Activation: PS@P(Py-$PyCOOH_0$) core/shell microspheres (0.60 g) were dispersed in 30 mL of deionized water under ultrasonication, and then the solutions of sodium citrate (0.12 g) and $PdCl_2$ (0.60 mL) (20.00 mmol/L, aq) were added in the dispersion. The pH value was adjusted to 6.5 by 0.2 M NaOH aqueous solution. $N_2H_4{\cdot}H_2O$ (0.10 mL) was added in the mixture as the reducing agent. The activated microspheres with Pd loaded on were precipitated and collected by centrifuging at 3000 r/min for 5 min. The PS@P(Py-$PyCOOH_{25-50}$)@Pd composite microspheres were synthesized as the same procedure but without the addition of sodium citrate. The PS@P(Py-PyCOOH)@Pd spheres were separated by centrifugation. (ii) Incorporation of Ni: The incorporation of nickel layer on the PS@P(Py-PyCOOH) microspheres was realized via electroless plating method but without the use of toxic tin salt. In a detailed description, the activated PS@P(Py-PyCOOH)@Pd particles, 0.55g of $NiSO_4{\cdot}6H_2O$, 3.36g of sodium tartaric ($Na_2C_4H_4O_6{\cdot}2H_2O$), 3.10 mL of $N_2H_4{\cdot}H_2O$, and 20.80 mL of deionized water were all added in a 50 mL round-bottom flask. The reaction mixture was stirred at 80 °C for 4 h. The centrifugation−redispersion cycles were repeated using deionized water as the dispersant until the washings were clear and colorless. 0.61 g of black powder was gotten after the composite microspheres of PS@P(Py-PyCOOH)@Ni were dried in a 60 °C oven for 24 h.

2.5. Characterization. The surface morphology of the synthesized microspheres was studied by field emission scanning electron microscope (SEM, HITACHI S-4700) at an acceleration voltage of 20 kV and the internal morphology was researched by transmission electron microscopy (TEM, HITACHI H-800) at an acceleration voltage of 200 kV and high-resolution transmission electron microscopy (HRTEM, JEOL 3010) at an acceleration voltage of 300 kV. The presence of Pd on the activated microspheres was ensured by energy dispersive X-ray (EDS, EDAX) spectroscopy. The incorporation of nickel nanocrystal on the spheres were confirmed by X-ray Photoelectron Spectroscopy (XPS, Thermo ESCALAB 250) and X-ray diffraction (XRD, Bruker D8 Advance, Cu Kα (λ = 1.5406 Å) radiation). The size and distribution of the microspheres was measured by Zetasizer NanoZS (Malvern). Thermogravimetric analyzer (TGA 4000, PerkinElmer) was carried out under nitrogen atmosphere at a heating rate of 10 °C/min. FTIR spectroscopy was recorded by BRUKER TENSOR 37. The magnetic measurements were carried out at room temperature using a vibrating sample magnetometer (VSM, Lakeshore 7410, USA) with a maximum magnetic field of 1 T. For the investigation of EM properties, permeability and permittivity parameters were measured on an HP8722ES network analyzer in the frequency range of 1−18 GHz. A sample containing 50 wt % of obtained products was pressed to the thickness of 2 mm for EM absorption measurement, and paraffin wax was used as the binder. The reflection losses were calculated using the measured electromagnetic data.

3. RESULTS AND DISCUSSION

3.1. Synthesis of Monodisperse PS@P(Py-PyCOOH) Core/Shell Microspheres. The uniform PS spheres had obtained through the dispersion polymerization. The SEM images of PS spheres suggests its smooth surface and diameter around 1.6 μm as shown in Figure 1a and Figure S1 in the Supporting Information. And the TEM image of PS spheres is shown in Figure S2. Moreover, the DLS results indicate the monomodal distribution of the ethanol dispersed PS spheres with PDI index at 0.021, as shown in Figure S3 in the Supporting Information. Meanwhile, the as-synthesized monodisperse PS spheres via dispersion polymerization were employed as the template for the further synthesis of PS@P(Py-PyCOOH) core/shell microspheres in this study. The oxidative polymerization of Py and PyCOOH was carried out using the PS microspheres as temples. In order to get a stable dispersion, Py was predissolved in ethanol together with small amount of CH_2Cl_2 and dropwisely added into the aqueous-ethanol dispersion of PS microspheres in the presence of PVP. A small amount of CH_2Cl_2 was used to swell the PS for Py penetration. The method is common for the situation that the water-soluble oxidant initiated polymerization of Py on the PS surface, and it is helpful to result in a smooth polymer coating. The prepenetration of shell monomer can improve the

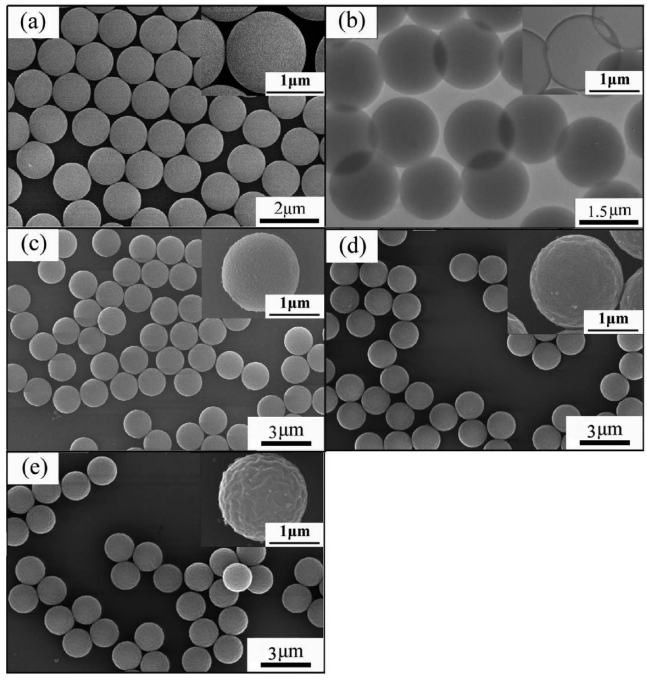

Figure 1. (a) SEM images of monodisperse PS seed, (b) TEM and (c) SEM images of PS/P(Py-$PyCOOH_0$) core/shell spheres, (d, e) SEM images of core shell structure microspheres with different PPyCOOH contents (d, 25%; e, 50%).

dx.doi.org/10.1021/am302551d | ACS Appl. Mater. Interfaces 2013, 5, 883−891

adhesion between the core and shell. The polymerization was initiated by adding $FeCl_3$. After six hours, PyCOOH was added with small amount of Py as the second batch of monomer in the aqueous solution form. Small amount of Py has to be added together with PyCOOH because only PyCOOH is hard to generate the high molecular weight homopolymer for the formation of a polymer shell with a certain mechanical strength. On the other hand, the small amount of Py copolymerized with PyCOOH in the second batch is used to improve the affinity between PPy buffer layer and P(Py-PyCOOH) layer.

The two-step feeding of monomers with the addition of PyCOOH during the second batch is essential to the stably formation and deposition of the P(Py-PyCOOH) on the surface of PS microspheres. If the PyCOOH was added with Py in one batch, it would be first initiated as soon as the addition of $FeCl_3$, which is due to the good solubility of PyCOOH in water. Meanwhile, color of the dispersion gradually turned to bown-gray during the polymerization process, which is the typical color of PPyCOOH homopolymer instead of the black color of PPy or P(Py-PyCOOH). However, due to high density of hydrophilic COOH groups, the PPyCOOH homopolymer would not prefer to deposit onto the hydrophobic surface of PS microspheres for the formation of continuous layers, as indicated by the corresponding SEM image in Figure S4 in the Supporting Information. Meanwhile, by using one batch PS@P(Py-$PyCOOH_{50}$) spheres for the further deposition of Ni, we can just obtain the PS@P(Py-$PyCOOH_{50}$)@Ni composite microspheres with a certain amount of irregular composites as suggested by the SEM image in Figure S5 in the Supporting Information. Therefore, the complete PS@P(Py-PyCOOH) core/shell microspheres can be only obtained via the two-step addition protocol with the addition of Py monomer in the first batch so as to form the PPy layer around the PS templates. As the surface affinity is much improved by the PPy layer, the copolymer of P(PyCOOH-*co*-Py) polymerized by the secondary batch of monomers is steadily deposited onto the outmost of surface of the microspheres.

The typical TEM image of the synthesized PS@P(Py-PyCOOH) microspheres is shown in Figure 1b, indicating that there is no isolated irregular deposition of PPy or PPyCOOH. The incorporation of P(Py-PyCOOH) shell on the surface of PS spheres is further confirmed by the inset of Figure 1b, where the P(Py-PyCOOH) hollow capsules are clearly shown after the PS core of PS@P(Py-PyCOOH) was dissolved by using CH_2Cl_2. The SEM images of the microspheres with different contents of PyCOOH are shown in Figure 1c−e. The diameters of PS@P(Py-$PyCOOH_{0,\ 25,\ 50}$) in Figure 1c−e are 1.74 ± 0.03 μm, 1.8 ± 0.03 μm, and 1.84 ± 0.04 μm, respectively. With the increasing PyCOOH content in P(Py-PyCOOH) shell, the diameter of the obtained core/shell microspheres was increased slightly. Moreover, the surface of the core/shell microspheres became more and more toughness. The surfaces of PS@P(Py-$PyCOOH_{50}$) spheres (Figure 1e) obviously show many wrinkles compared with the slightly coarse surface of PS@P(Py-$PyCOOH_0$) (Figure 1c), which is due to the P(Py-PyCOOH) shell layer with the increased PyCOOH content being partially swelled by the medium, and its surface would in turn shrink as the solvent evaporated.

3.2. Synthesis of PS@P(Py-PyCOOH)@Ni Composite Microspheres. Ni was further deposited onto the surface of the conductive polymer of the PS@P(Py-PyCOOH) core/shell spheres to prepare the PS@P(Py-PyCOOH)@Ni composite microspheres via the electroless plating technique. First, the PS@P(Py-PyCOOH) core/shell spheres were activated with nano-Pd, which was in situ produced via the reduction of $PdCl_2$ by $N_2H_4{\cdot}H_2O$. The PyCOOH units on the outmost surface of the P(Py-PyCOOH) shell layer provide carboxyl groups and served as the effective binding sites for the loading of nano-Pd during the activation reaction process. For the sample of PS@P(Py-$PyCOOH_0$), additional sodium citrate salt is used in the activation step which is an usually used dopant and can also provide carboxylic acid groups as the active sites for the deposition of nanometals after it has been doped with the PPy layer.[33,51]

For the incorporation of nanometal on the copolymer, metal such as Ni can be directly added in the system in the form of nanoparticles or produced by in situ reduction. The direct addition of Ni powder into the Py polymerization would give out Ni@PPy nanocomposites which have been reported by Xu et al.[38] Although microstructured Ni@PPy core/shell composites were obtained in that work, the morphology of the products is amorphous and uniform spheres are hardly to be prepared by the method adding Ni nanoparticle directly because the nano Ni is very easy to cluster. Instead we choose the in situ reduction method to introduce nanometal, which is also an general method to produce polymer@nanometal with regular morphologies like core/shell spheres.[52]

In the design of the in situ reduction, it is worth noting that the redox potential of Ni^{2+}/Ni is not high enough to be directly reduced by hydrazine at moderate reaction conditions as presented in this work. In the early exploration, we have carried out two experimental with Ni^{2+} reduced at similar conditions using surface-modified PS microspheres as the templates. In the experimental without Pd catalyst (direct reduction), the color of the reaction mixture did not even change (no reaction) and no Ni can be observed on the PS surfaces (shown in Figure S7 in the Supporting Information). However, in the experimental with the PS microspheres preactivated by nano-Pd (activation-electroless plating method), typical Ni nanocrystals can be observed tightly surround the PS spheres. So in this work, we choose the activation-electroless method for the deposition of Ni. The Pd nanoparticles loading on the microspheres via the activation step can not only catalysis the reduction of Ni^{2+}, but also guarantee the tailored growth of the Ni crystals.

The EDS results as well as the HRTEM image of the Pd-activated microspheres were shown in Figure 2, in which the dark dots indicate the loading of nano-Pd on the PS@P(Py-PyCOOH) microspheres. In the EDS spectrum, the weak peak around 21 keV is due to the Pd presence, which further confirmed the loading of Pd on the PS@P(Py-PyCOOH) microspheres. The existence of Cu and Fe is caused by the Cu grid used and the pollution in polar field, respectively. Meanwhile, the presence of Pd can also be proved by the peak at 337.8 eV in the XPS spectrum as shown in Figure 4b, which is the electron peak of Pd3d.

The Pd-activated spheres were then dispersed in the electroless plating solution batch where the Pd-catalyzed reduction of Ni^{2+} occurred. The loading of Pd on the microspheres can make the reduction reaction mainly surround the activated microspheres so as that the produced Ni would attach on the surface of microspheres to form the composite microspheres. The SEM images of the composites with different PyCOOH content at 0, 25, and 50% are shown in Figure 3a−c, respectively. It is found in Figure 3a that small aloelike Ni crystals with the diameter of about 100 nm can be obtained, confirming the successful reduction from Ni^{2+} to Ni.

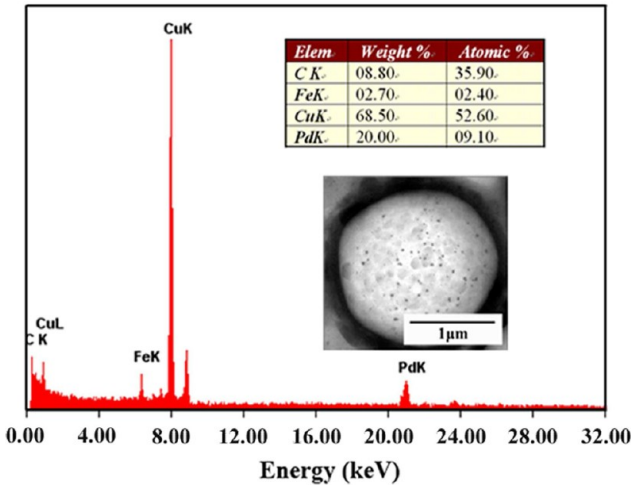

Figure 2. EDS spectrum of hollow PS@P(Py-PyCOOH) microspheres with Pd on the surface, inset: HRTEM images of Pd activated hollow PS@P(Py-PyCOOH) microspheres.

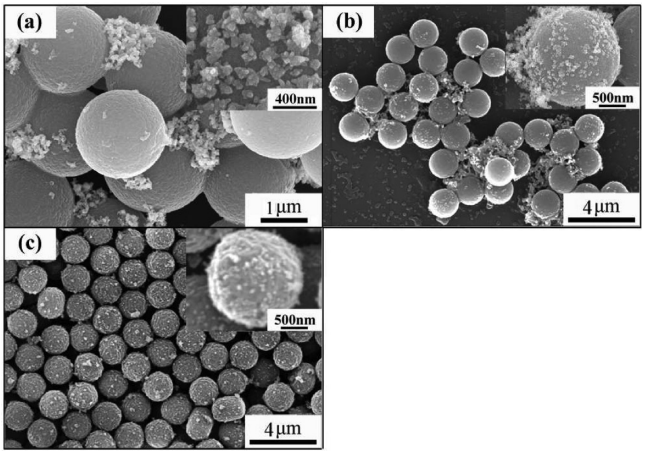

Figure 3. SEM images of (a) PS@P(Py-PyCOOH$_0$)@Ni, (b) PS@P(Py-PyCOOH$_{25}$)@Ni and (c) PS@P(Py-PyCOOH$_{50}$)@Ni core/shell microspheres.

However, most of such metal crystals aggregate together and irregular distribute among the PS@P(Py-PyCOOH$_0$) microspheres. And only a few of the Ni crystals are attached on the microspheres, which can also be proved by TEM image as shown in Figure S6 in the Supporting Information. When the content of PyCOOH increased to 25%, the coverage of Ni on the surface of the PS@P(Py-PyCOOH$_{25}$) microspheres are correspondingly increased as shown in Figure 3b. Moreover, large amounts of the isolated Ni aggregates can still be observed surrounding the microspheres. The complete Ni layer can be obtained with the content of PyCOOH at 50%, as indicated by the SEM image in Figure 3c. And the as-synthesized composite microspheres were raspberry-like with the uniformly deposited Ni onto the surface. The Ni nanocrystal in PS@P(Py-PyCOOH$_0$)@Ni sample cluster together. Therefore, the average diameters of this kind of spheres will be pointless. Furthermore, the average diameters of PS@P(Py-PyCOOH$_{25,\ 50}$)@Ni in Figure 3b, c are 1.86 ± 0.12 μm and 1.96 ± 0.10 μm, respectively. Experiments for the further increase in PPyCOOH contents were also attempted but failed in this study. The layer of P(Py-PyCOOH) with the PyCOOH content higher than 50% would dissolve in the reducing bath during the Pd activation and/or Ni deposition process, in which the solution was alkaline. As the PyCOOH content up to 60%, its SEM image in Figure S8 in the Supporting Information indicated the decrease in Ni coverage on the spheres surfaces.

The typical XRD pattern of the as-synthesized PS@P(Py-PyCOOH)@Ni composite is shown in Figure 4a. The

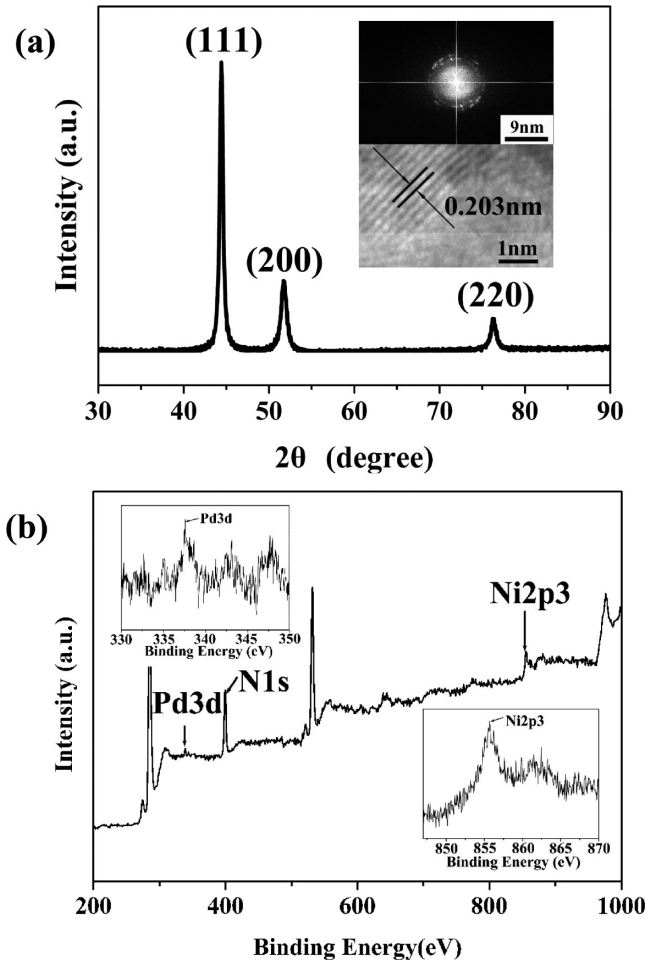

Figure 4. (a) XRD spectrum of PS@P(Py-PyCOOH$_0$)@Ni core shell particles, lower inset: high-resolution lattice image and upper inset: corresponding FFT pattern (inset) of the nickel shell (b) X-ray photoelectron spectra (XPS) of the Ni deposited after activation. Inset: high-resolution XPS Pd3d and Ni2p3 spectra.

diffraction peaks indicate the crystallization of the Ni nanoparticles, which are due to the face-centered cubic (FCC) phase of Ni (PDF: 70−1849, space group $Fm\bar{3}m$). The diffraction peaks at 2θ = 44.48, 51.83, and 76.35° are assigned as the (111), (200), and (220) planes. Meanwhile, the HRTEM image of the lattice fringes of the Ni nanocrystals is shown in of Figure 4a, indicating that the lattice spacing is 0.203 nm attributed to the (111) lattice plane of Ni FCC crystal. The crystal structure of the Ni nanoparticle is also suggested by the diffraction spots in the ED pattern as shown in Figure 4a. These results strongly indicate the successfully loading of Ni nanoparticles around the PS@P(Py-PyCOOH) microspheres. Meanwhile, the XPS spectra of the as-synthesized PS@P(Py-PyCOOH)@Ni composites are also measured as shown in Figure 4b. The binding energy peak at 857.7 eV for Ni2p3 further supported the presence of Ni, which is consistent with the XRD and HRTEM results. Also in the XPS spectrum,

dx.doi.org/10.1021/am302551d | ACS Appl. Mater. Interfaces 2013, 5, 883−891

the binding energy at 399.8 eV is confirmed the N1s from PPy and PPyCOOH.[53]

The TGA curves of the as-prepared PS@P(Py-PyCOOH)@Ni composites are shown in Figure 5. The effective loading of

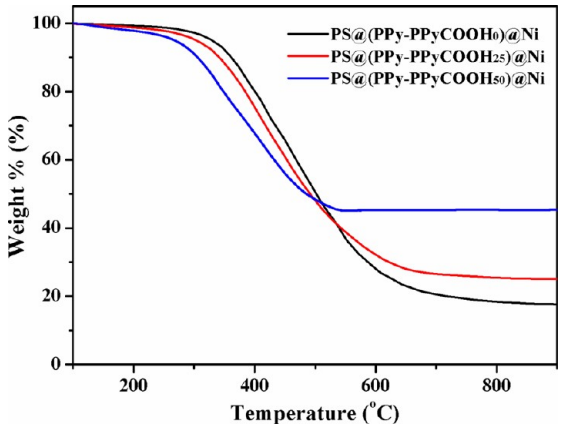

Figure 5. TGA curves of PS@P(Py-PyCOOH$_{0,\ 25,\ 50}$)@Ni core/shell microspheres.

Ni on the composite can be determined by the residual weight at 800 °C, which were about 45, 25, and 18% for PS@P(Py-PyCOOH$_{50}$)@Ni, PS@P(Py-PyCOOH$_{25}$)@Ni and, PS@P(Py-PyCOOH$_0$)@Ni, respectively. The results revealed in Figure 5 obtained by TGA are in consistent with the results revealed in Figure 3 obtained by SEM images with the increase of PyCOOH content in the P(Py-PyCOOH) layer. And in the temperature range from 350 to 470 °C, three samples show parallel weight loss curves, indicating the similar decomposition rates. Moreover, the onset of the decomposition temperature decreases from 334 to 291 °C, which is partially due to the increasing content of PyCOOH from 0 to 50%, during the synthesis of conductive polymer layer because the PPyCOOH is less thermally stable than the pristine PPy. Therefore, TGA results indicate that the increase of PyCOOH content in the P(Py-PyCOOH) layer can effectively enhance the loading of Ni particles on the surface of PS@P(Py-PyCOOH) microspheres.

3.3. Magnetic Properties of PS@P(Py-PyCOOH)@Ni Composite Microsphere. The magnetic properties of the PS@P(Py-PyCOOH)@Ni composite microspheres as a function of PyCOOH content in the P(Py-PyCOOH) layer were determined by VSM analysis at 300 K, and their hysteresis loops are shown in Figure 6 with a enlarged part within ±0.5 Oe region. It is striking to note that all the composites behave as a slender hysteresis loop at the temperature of 300 K, indicating the ferromagnetic behavior of them. The results of their saturation magnetization (M_s), residual magnetism (M_r), and coercivity (H_c) are summarized in Table 2 with the comparison of pure Ni powder.[38] The both M_s and M_r of the composite microspheres obviously increase with the content of PyCOOH, which is due to the increasing amount of loaded Ni around the PS@(Py-PyCOOH) microspheres. The Ni loading on the composite spheres is stabilized by the carboxylic groups introduced by the copolymerization of PyCOOH in the composite spheres. The more PyCOOH used, the higher the correspondingly carboxyl acid content on the sphere surface, the higher content of Ni can be loaded on the composite particles. As Ni content has positive contribution on M_s, it is reasonable for us to observe the increasing M_s of the composites with the increasing content of PyCOOH. And

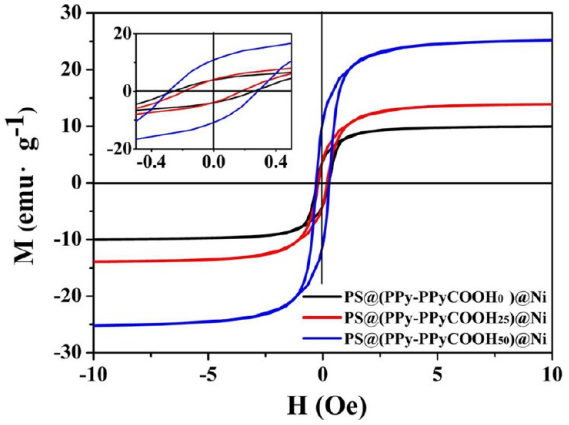

Figure 6. Hysteresis loops measured at room temperature for PS@P(Py-PyCOOH$_{0,\ 25,\ 50}$)@Ni microspheres.

these results are consistent with those of TGA as shown in Figure 5. The results of M_s and M_r were further normalized by the weight of Ni and listed in Table 2, which are designed as M_s^0 and M_r^0 hereafter. The normalized M_s observed on such samples of PS@P(Py-PyCOOH$_{0,25,50}$)@Ni is near 55 emu g^{-1}, very close to the M_s of pure nickel powder. The almost same M_s^0 values observed in Table 2, after the M_s values have been normalized by Ni content, can further prove that the increasing M_s is coming from the increasing Ni content. But both the M_r^0 and H_c of the nickel crystals composited on microspheres are much enhanced than Ni powder, which can possibly indicate the different magnetic domain state caused by the special Ni structure tailored by the carboxylic acid groups on the conductive polymer surface of the composite spheres.[54]

3.4. EM Properties of PS@P(Py-PyCOOH)@Ni Composite Microspheres. The EM properties of the PS@P(Py-PyCOOH$_{0,25,50}$)@Ni composites and the PS@P(Py-PyCOOH$_0$) core/shell microspheres were investigated in the frequency range from 1 to 18 GHz in this study. The real (μ') and the imaginary (μ'') parts of the relative complex permeability are shown in panels a and b in Figure 7, respectively, together with the tangent magnetic loss angle (tan δ_M) of the composites in Figure 7c. It is noted in Figure 7a−c that the as-synthesized PS@P(Py-PyCOOH)@Ni composites with different PyCOOH content in the P(Py-PyCOOH) layer show the similar frequency-dependent permeability. As shown in Figure 7a, the three curves of μ' as a function of frequency intersect at 10 GHz, and they obviously increase in the order of PS@P(Py-PyCOOH$_{25}$)@Ni, PS@P(Py-PyCOOH$_0$)@Ni and PS@P(Py-PyCOOH$_{50}$)@Ni as the frequency lower than the intersection point. Meanwhile, after the intersection, all of the three curves behave as obvious elevation in the frequency range from 10 to 18 GHz. For the variations in μ'' as a function of frequency shown in Figure 7b, there is an obvious valley in the frequency range from 4 to 12 GHz for each composite. Moreover, the highest μ'' is also obtained for PS@P(Py-PyCOOH$_{50}$)@Ni, indicating the highest magnetic loss in both the low frequency range from 1 to 4 GHz and the high frequency range from 12 to 18 GHz. The energy loss caused by magnetic relaxation can be more clearly evaluated by tan δ_M, which is also plotted as a function of frequency as shown in Figure 7c. The shapes and the tendencies of the tan δ_M vs frequency are almost the same with those of the μ'' vs frequency. The increase of tan δ_M with the increasing PyCOOH content in the P(Py-PyCOOH) layer in the low frequency

Table 2. Magnetic Properties of PS@P(Py-PyCOOH)@Ni Composites Measured at 300 K

sample	M_s (emu g^{-1})	M_r (emu g^{-1})	M_r/M_s	H_c(Oe)	M_s^0 (emu g^{-1})^b	M_r^0 (emu·g^{-1})^b
PS/P(Py-$PyCOOH_0$)/Ni	10.0	4.9	0.49	264	55.6	27.2
PS/P(Py-$PyCOOH_{25}$)/Ni	14.0	5.4	0.38	186	56.0	21.6
PS/P(Py-$PyCOOH_{50}$)/Ni	24.5	12.5	0.51	286	54.4	27.8
Ni^a			0.031	0.7	55.9	1.75

^{a}The data are from ref 38. ^{b}Normalized by the neat Ni weight obtained from TGA data.

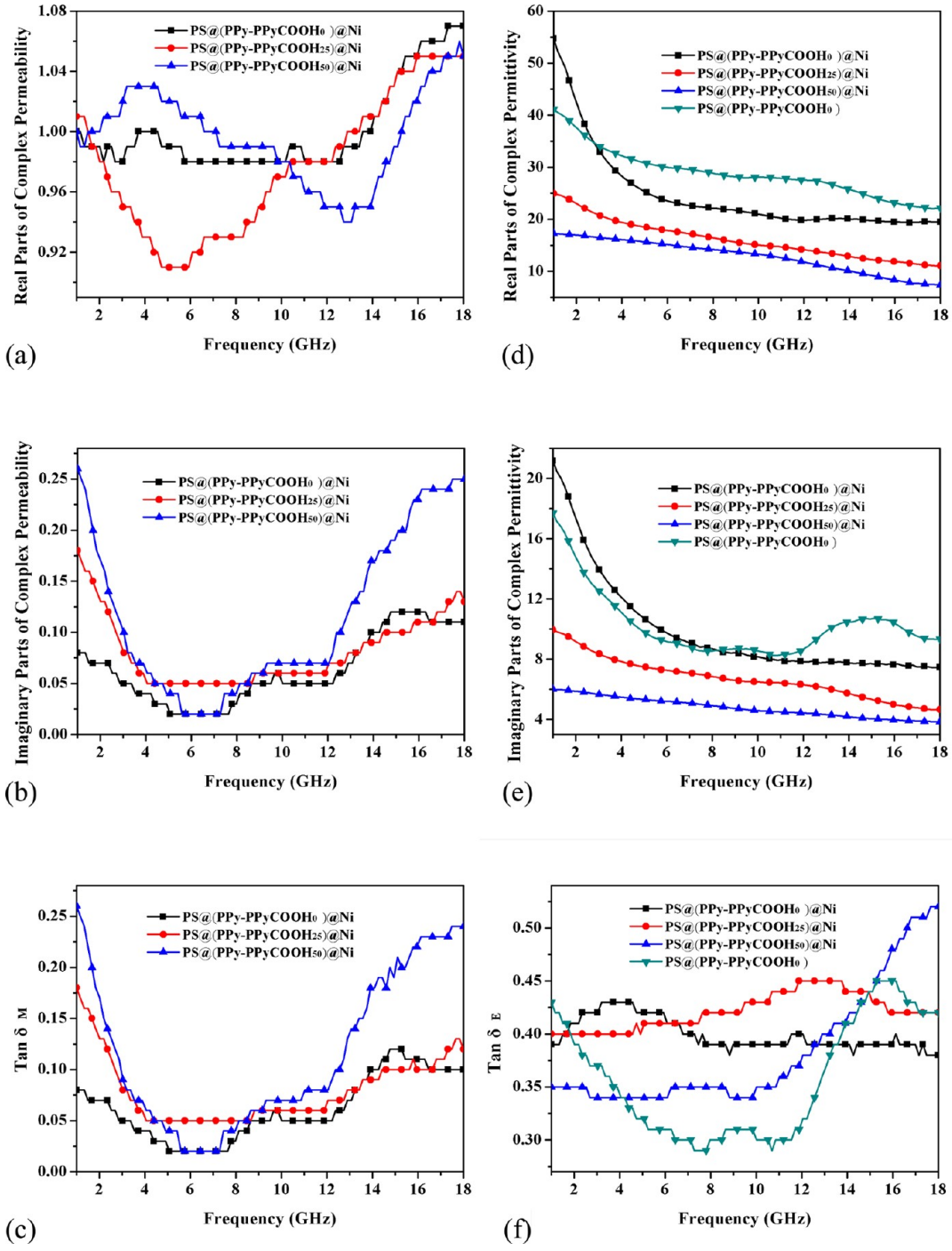

Figure 7. (a) Real (μ') and (b) imaginary (μ'') parts of the relative complex permeability of PS@P(Py-$PyCOOH_{0,\ 25,\ 50}$)@Ni core/shell microspheres in the frequency range of 1−18 GHz, (c) tangent δ_M loss of PS@P(Py-$PyCOOH_{0,\ 25,\ 50}$)@Ni spheres. (d) Real (ε') and (e) imaginary (ε'') parts of the relative complex permittivity of PS@P(Py-$PyCOOH_{0,\ 25,\ 50}$)@Ni and PS@P(Py-$PyCOOH_0$) core/shell microspheres in the frequency range of 1−18 GHz, (f) tangent δ_E loss of PS@P(Py-$PyCOOH_{0,\ 25,\ 50}$)@Ni and PS@P(Py-$PyCOOH_0$) core/shell microspheres.

dx.doi.org/10.1021/am302551d | ACS Appl. Mater. Interfaces 2013, 5, 883−891

region is due to the corresponding increase of Ni content on the surface composite microspheres. However, in the high-frequency region, there is no obvious difference between PS@P(Py-PyCOOH$_0$)@Ni and PS@P(Py-PyCOOH$_{25}$)@Ni, and the remarkable increase of tan δ_M for PS@P(Py-PyCOOH$_{50}$)@Ni from 14 to 18 GHz is possibly attributed to the formation of complete Ni layer out of the core/shell microspheres.

The variation in ε', ε'', and the tangent of dielectric loss angle (tan δ_E) as a function of frequency of the composites are shown in Figure 7d–f, respectively. Meanwhile, the dielectric results of PS@P(Py-PyCOOH$_0$) core/shell microspheres are also displayed in panels d and e in Figure 7. It is clearly shown that both ε' and ε'' slowly decreases with frequency, which become more remarkable with the increase in PyCOOH content in the P(Py-PyCOOH) layer. Moreover, compared with the PS@P(Py-PyCOOH$_0$)@Ni composite microspheres, the PS@P(Py-PyCOOH$_0$) microspheres behave as the higher ε' and comparable ε'', indicating that the incorporation of Ni can depress ε', whereas the copolymerization of PyCOOH can induce the decrease of ε'' for the composites. As displayed in Figure 7f, the two kinds of complete core/shell microspheres of PS@P(Py-PyCOOH$_0$) and PS@P(Py-PyCOOH$_{50}$)@Ni show the similar elevating trend of tan δ_E within the frequency range from 6 to 18 GHz. However, the value of tan δ_E for PS@(Py-PyCOOH$_0$) slowly decreases with frequency in the low frequency region from 0 to 6 GHz, which is different from that of tan δ_E for PS@P(Py-PyCOOH$_{50}$)@Ni. Besides, the maximum of tanδ_E for PS@P(Py-PyCOOH$_0$) emerges around 16 GHz, which is lower than that of tan δ_E for PS@P(Py-PyCOOH$_{50}$)@Ni around 18 GHz. For PS@P(Py-PyCOOH$_0$)@Ni and PS@P(Py-PyCOOH$_{25}$)@Ni, even though the variations in tan δ_E are relatively flat around 0.4, the peaks can still be observed at 4 and 13 GHz, respectively. The steady right-shift of tanδ_E peaks from 4, 13, to 18 GHz with the increasing PyCOOH content from 0 to 25 to 50% is expected to be caused by the correspondingly increasing Ni loadings on the composite spheres, which can be explained by the interfacial dielectric relaxation of PPy and Ni phases.[45]

As the EM adsorption performance depends on not only the loss of magnetic and dielectric but also the proper matching of the dielectric and the magnetic properties, the final EM efficiency of the as-synthesized composite microspheres were evaluated by the reflection loss of the samples based on transmission line theory.[55] According to this theory, when the EM wave transmits through a medium, there are many factors affected the reflectivity, such as μ, ε, sample thickness, and EM wave frequency. The reflection loss of the EM wave (R) can be expressed as

$$R\ (\mathrm{dB}) = 20\log|(Z-1)/(Z+1)| \quad (1)$$

The input impedance at the surface, Z is given by

$$Z = (\mu_r/\varepsilon_r)^{1/2}\tanh[j(2\pi fd/c)(\mu_r\varepsilon_r)^{1/2}] \quad (2)$$

where f is the frequency of the EM wave, c is the velocity of light in free space, and d is the thickness of the absorber layer.

So the R of composite microspheres can be calculated with the curves of R vs frequency as shown in Figure 8. Compared with PS@P(Py-PyCOOH$_0$) composites, the peak position of R in PS@P(Py-PyCOOH$_0$)@Ni sample shifts from 6.95 to 7.97 GHz, and the peak width at R = −10 dB grows from 0.85 to 1.19 GHz. The peak width of reflection loss increases, which indicates an enhanced behavior after Ni deposition. The

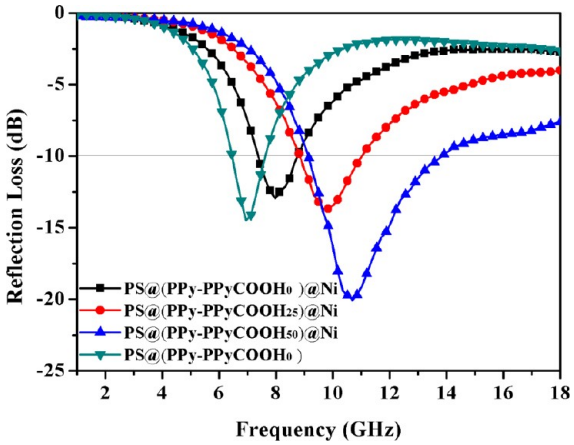

Figure 8. Calculated reflection loss of PS@P(Py-PyCOOH$_{0,\ 25,\ 50}$)@Ni and PS@P(Py-PyCOOH$_0$) composite spheres.

reflection loss peaks of the PS@P(Py-PyCOOH)@Ni composites shows the obvious movement to high frequency region and broadening peak width with the increasing contents of Ni. The peak values of R for PS@P(Py-PyCOOH$_{0,25,50}$)@Ni spheres are −12.93, −13.69, −20.06 at 7.97, 9.67, 10.69 GHz, respectively. And the minimum value is obtained for PS@P(Py-PyCOOH$_{50}$)@Ni with the EM absorption less than −10 dB in the frequency region from 9.16 to 13.75 GHz.

4. CONCLUSION

In summary, a novel method for fabricating PS@P(Py-PyCOOH)@Ni composite core/shell microspheres was brought forward. By proper introducing PyCOOH as the comonomer, we got uniform and complete PS@P(Py-PyCOOH)@Ni core/shell structures through an in situ oxidative polymerization followed by the electroless plating process. The electroless plating method can effectively increases the incorporation contents of Ni onto the PS@P(Py-PyCOOH) microspheres, confirmed by TGA and hysteresis loss characterization. The prepared PS@P(Py-PyCOOH$_{0,\ 25,\ 50}$)@Ni spheres behaves as ferromagnetic material and good EM absorption performance. The formation of uniformed Ni shell structure enhances the absorption performance. The electromagnetic absorption less than −10 dB is found in 9.16–13.75 GHz range for the PS@P(Py-PyCOOH$_{50}$)@Ni composite microspheres with the minimum reflection loss reached −20.06 dB at 10.69 GHz. Moreover, the reflection loss peaks moves steady from the low-frequency to hig- frequency range with the increasing PyCOOH content from 0 to 50%. Therefore, relay on the enough carboxyl groups, the successful electroless deposition is confirmed a good method to in the preparation of our PS@P(Py-PyCOOH$_{50}$)@Ni composite microspheres. The obtained ferromagnetic and EM wave absorbable composite microspheres have potential applications as effective additives for the electromagnetic absorbing materials.

■ ASSOCIATED CONTENT

Supporting Information

SEM, TEM, and DLS results of monodispersed PS spheres. The SEM figures of PS@P(Py-PyCOOH$_{50}$)* and PS@P(Py-PyCOOH$_{50}$)*@Ni spheres synthesized in one batch are shown in S4 and S5. Figure S6 is the TEM result of PS@P(Py-PyCOOH0)@Ni microspheres. Figure S7 is the SEM figure of PS@Ni spheres without the copolymer layer. Figure S8 shows

the SEM images of PS@P(Py-PyCOOH$_{60}$)@Ni spheres. This material is available free of charge via the Internet at http://pubs.acs.org/.

AUTHOR INFORMATION

Corresponding Author

*E-mail: qiuteng@mail.buct.edu.cn (T.Q.); lixy@mail.buct.edu.cn (X.Y.L.).

Notes

The authors declare no competing financial interest.

ACKNOWLEDGMENTS

The authors are grateful for the financial support from the National Natural Science Foundation of China (Grant 50703002) the Fundamental Research Funds for the Central Universities (Grant JD1108).

REFERENCES

(1) Wu, G.; More, K. L.; Johnston, C. M.; Zelenay, P. *Science* **2011**, *332*, 443−447.
(2) Zhang, Y.; Wang, H.; Kräemer, S.; Shi, Y.; Zhang, F.; Snedaker, M.; Ding, K.; Moskovits, M.; Snyder, G. J.; Stucky, G. D. *ACS Nano* **2011**, *5* (4), 3158−3165.
(3) Yang, C.; Liu, P.; Wang, T. *ACS Appl. Mater. Interfaces* **2011**, *3* (4), 1109−1114.
(4) Hall, S. R.; Davis, S. A.; Mann, S. *Langmuir* **2000**, *16*, 1454−1456.
(5) Pan, J. H.; Zhang, X. W.; Du, A. J.; Darren, D. S.; James, O. L. *J. Am. Chem. Soc.* **2008**, *130*, 11256−11257.
(6) Zhang, L.; Wu, J. J.; Wang, Y. X.; Long, Y. H.; Zhao, N.; Xu, J. *J. Am. Chem. Soc.* **2012**, *134*, 9879−9881.
(7) Song, H. Z.; Li, Y. X.; Zeng, J. T.; Li, G. R.; Yin, Q. R. *J. Magn. Mater.* **2008**, *320*, 978−982.
(8) An, Z. G.; Pan, S. L.; Zhang, J. J. *J. Phys. Chem. C* **2009**, *113*, 2715−2721.
(9) Chen, M.; Zhou, J.; Xie, L.; Gu, G. X.; Wu, L. M. *J. Phys. Chem. C* **2007**, *111*, 11829−11835.
(10) Li, J. Y.; Xiong, S. L.; Pan, J.; Qian, Y. T. *J. Phys. Chem. C* **2010**, *114*, 9645−9650.
(11) Claro, P. C.; Castez, M. F.; Schilardi, P. L.; Luque, N. B.; Leiva, E. P.; Salvarezza, R. C. *ACS Nano* **2008**, *2*, 2531−2539.
(12) Mangeney, C.; Bousalem, S.; Connan, C.; Vaulay, M. J.; Bernard, S.; Chehimi, M. M. *Langmuir* **2006**, *22*, 10163−10169.
(13) Xuan, S. H.; Wang, Y. X.; Leung, K. C.; Shu, K. *J. Phys. Chem. C* **2008**, *112*, 18804−18809.
(14) Du, J. J.; Jing, C. Y. *J. Phys. Chem. C* **2011**, *115*, 17829−17835.
(15) Song, D.; Zhou, J. D.; Jiang, W.; Zhang, X. J.; Yan, Y.; Li, F. S. *Mater. Lett.* **2009**, *63*, 282−284.
(16) Zhu, J. H.; Pallavkar, S.; Chen, M. J.; Yerra, N.; Luo, Z.; Colorado, H. A.; Lin, H.; Haldolaarachchige, N.; Khasanov, A.; Ho, T. C.; Young, D. P.; Wei, S.; Guo, Z. *Chem. Commun.* **2013**, *49*, 258−260.
(17) Zhang, X.; Wei, S.; Haldolaarachchige, N.; Colorado, H. A.; Luo, Z.; Young Da., P.; Guo, Z. *J. Phys. Chem. C* **2012**, *116*, 15731−15740.
(18) Chen, X.; Wei, S.; Gunesoglu, C.; Zhu, J.; Southworth, C. S.; Sun, L.; Karki, A. B.; Young, D. P.; Guo, Z. *Macromol. Chem. Phys.* **2010**, *211*, 1775−1783.
(19) Zhu, J.; Wei, S.; Haldolaarachchige, N.; Young, D. P.; Guo, Z. *J. Phys. Chem. C* **2011**, *115*, 15304−15310.
(20) Wei, S.; Wang, Q.; Zhu, J.; Sun, L.; Lin, H.; Guo, Z. *Nanoscale* **2011**, *3*, 4474−4502.
(21) Cravillon, A.; Nayuk, R.; Springer, S.; Feldhoff, A.; Huber, K.; Wiebcke, M. *Chem. Mater.* **2011**, *23* (8), 2130−2141.
(22) Goswami, L.; Sarma, S. N.; Chowdhury, D. *J. Phys. Chem. C* **2011**, *115* (40), 19668−19675.
(23) Zhang, J. R.; Qiu, T.; Yuan, H. F.; Shi, W. Z.; Li, X. Y. *Mater. Lett.* **2011**, *65*, 790−792.
(24) Sang, A. J.; Kim, K.; Kim, J. H.; Lee, S. S. *ACS Appl. Mater. Interfaces* **2011**, *3* (8), 2904−2911.
(25) Yao, K. X.; Hua Chun, Z. *Chem. Mater.* **2012**, *24* (1), 140−148.
(26) Li, Y.; Kim, Y. J.; Kim, A. Y.; Lee, K.; Jung, M. H.; Hur, N. H.; Park, K. H.; Seo, W. S. *Chem. Mater.* **2011**, *23* (24), 5398−5403.
(27) Ren, B.; Ruditskiy, A.; Song, J. H.; Kretzschmar, I. *Langmuir* **2012**, *28* (2), 1149−1156.
(28) Wang, C.; Han, X.; Xu, P.; Wang, J.; Du, Y.; Wang, X.; Qin, W.; Zhang, T. *J. Phys. Chem. C* **2010**, *114* (7), 3196−3203.
(29) Chen, M.; Xie, L.; Li, F.; Zhou, S.; Wu, L. *ACS Appl. Mater. Interfaces* **2010**, *2* (10), 2733−2737.
(30) Parambhath, V. B.; Nagar, R.; Sethupathi, K.; Ramaprabhu, S. *J. Phys. Chem. C* **2011**, *115* (31), 15679−15685.
(31) He, F.; Yang, P.; Wang, D.; Li, C.; Niu, N.; Gai, S.; Zhang, M. *Langmuir* **2011**, *27* (9), 5616−5623.
(32) Yuan, J. J.; Zhou, S. X.; Wu, L. M.; You, B. *J. Phys. Chem. B* **2006**, *110*, 388−394.
(33) Arunagiri, T.; Golden, T. D.; Chyan, O. *Mater. Chem. Phys.* **2005**, *92*, 152−158.
(34) Nobukawa, S.; Urakawa, O.; Shikata, T.; Inoue, T. *Macromolecules* **2010**, *43*, 6099−6105.
(35) Pol, V. G.; Grisaru, H.; Gedanken, A. *Langmuir* **2005**, *21*, 3635−3640.
(36) Xia, Y.; Yang, P.; Sun, Y.; Wu, Y.; Mayers, B.; Gates, B. *Adv. Mater.* **2003**, *15*, 353−389.
(37) Bai, M. Y.; Cheng, Y. J.; Wickline, S. A.; Xia, Y. *Small* **2009**, *5*, 1747−1752.
(38) Xu, P.; Han, X. J.; Wang, C.; Zhou, D. H.; Lv, Z. S.; Wen, A. H. *J. Phys. Chem. B* **2008**, *112*, 10443−10448.
(39) Yuan, X.; Zeng, X.; Zhang, H. J.; Ma, Z. F.; Wang, C. Y. *J. Am. Chem. Soc.* **2010**, *132* (6), 1754−1755.
(40) Wang, Y. Q.; Zou, B. F.; Gao, T.; Wu, X. P.; Lou, S. Y.; Zhou, S. M. *J. Mater. Chem.* **2012**, *22* (18), 9034−9040.
(41) Zhao, B. B.; Nan, Z. D. *J. Magn. Magn. Mater.* **2012**, *324* (15), 2380−2387.
(42) Luo, Y. L.; Fan, L. H.; Xu, F.; Chen, Y. S.; Zhang, C. H.; Wei, Q. B. *Mater. Chem. Phys.* **2010**, *120* (2−3), 590−597.
(43) Callegari, V.; Demoustier-Champagne, S. *ACS Appl. Mater. Interfaces* **2010**, *2* (5), 1369−1376.
(44) Zhou, W.; Hu, X.; Bai, X.; Zhou, S.; Sun, C.; Yan, J.; Chen, P. *ACS Appl. Mater. Interfaces* **2011**, *3* (10), 3839−3845.
(45) Xu, Z.; Li, C.; Kang, X.; Yang, D.; Yang, P.; Hou, Z.; Lin, J. *J. Phys. Chem. C* **2010**, *114* (39), 16343−16350.
(46) Montoya, P.; Jaramillo, F.; Calderon, J.; Torresi, S.; Torresi, R. M. *Electrochim. Acta* **2010**, *55* (21), 6116−6122.
(47) Zhang, J.; Qiu, T.; Ren, S.; Yuan, H.; He, L.; Li, X. *Mater. Chem. Phys.* **2012**, *134* (2−3), 1072−1078.
(48) Lee, J. W.; Serna, F.; Nickels, J.; Schmidt, C. E. *Biomacromolecules* **2006**, *7*, 1692−1695.
(49) Shi, W.; Cao, H.; Shen, Y.; Song, C.; Li, D.; Zhang, Y.; Ge, D. *Macromol. Chem. Phys.* **2009**, *210* (17), 1379−1386.
(50) Okubo, M.; Minami, H.; Yamamoto, Y. *Colloids Surf., A* **1999**, *153*, 405−411.
(51) Lu, Y.; Mei, Y.; Schrinner, M.; Ballauff, M.; Maller, M. W.; Breu, J. *J. Phys. Chem. C* **2007**, *111*, 7676−7681.
(52) Xu, J.; Hu, J.; Quan, B.; Wei, Z. *Macromol. Rapid Commun.* **2009**, *30*, 936−940.
(53) Kang, E. T.; Neoh, K. G.; Zhang, X.; Tan, K. L.; Liaw, D. J. *Surf. Interface Anal.* **1996**, *24*, 51−58.
(54) Yi, R.; Shi, R.; Gao, G.; Zhang, N.; Cui, X.; He, Y.; Liu, X. *J. Phys. Chem. C* **2009**, *113*, 1222−1226.
(55) Michielssen, E.; Sajer, J.; Ranjithan, S.; Mittra, R. *IEEE Trans. Microwave Theory Technol.* **1993**, *41*, 1024.